ACS Partner Journal

ENVIRONMENT & HEALTH

Open Access

pubs.acs.org/EnvHealth

Article

Multidimensional Unraveling Insights from an Enzyme-Nanozyme Cascade-Based Electrochemical Biosensor for Screening Microplastic Neurotoxicity

Published as part of Environment & Health special issue "Transforming Environmental Exposure and Health Research through Emerging Technologies".

Yifei Xing, Xuehan Wei, Xu Liang, and Huimin Zhao*

Cite This: *Environ. Health* 2026, 4, 1151−1161

Read Online

ACCESS | Metrics & More | Article Recommendations | Supporting Information

ABSTRACT: Accurate quantification of biomarkers is crucial for evaluating the neurotoxicity of pollutants. Traditional detection methods, albeit important, are limited by single analytical indicators and time-consuming procedures, which lead to distorted detection results for biomarkers with high metabolic rates. Herein, a multiplexed electrochemical sensing array was designed based on nanozyme capsules; this metal-porphyrin-structured covalent−organic framework embedded with enzymes simultaneously detected H_2O_2, acetylcholine (ACh), and glucose (Glu). The nanozyme capsule not only exhibits peroxidase-like activity for the sensitive detection of H_2O_2 but also serves as a carrier to encapsulate enzymes within its cavities, forming a cascade catalytic system for the specific recognition of ACh or Glu. This sensor features a broad detection range, low detection limits, and a strong anti-interference capability. More importantly, it can rapidly quantify three easily degradable biomarkers in neuronal lysates within 3 min without pretreatment. With the sensor, we multidimensionally assessed and differentiated the effects of different microplastics (MPs) based on the ability of neurons to produce ACh and H_2O_2 as well as their glucose uptake capacity. Furthermore, it is found that MPs induce stronger neurotoxic effects under hyperglycemia. This study not only provides an effective tool for determining multiple easily degradable biomarkers but also offers technical support for assessing the health risks of pollutants.

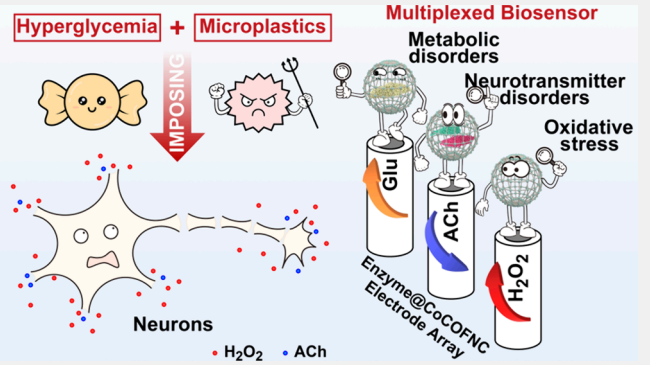

KEYWORDS: *Microplastics, Neurotoxic effect, Multidimensional analysis, Electrochemical biosensor, Hyperglycemia, Nanozyme*

INTRODUCTION

Microplastics (MPs), plastic particles <5 mm in diameter, are ubiquitous in water, air, and soil, posing ecological and health risks.[1] Upon human exposure, MPs can affect multiple physiological systems; neurotoxicity is of particular concern.[2] MPs elevate reactive oxygen species (ROS), inducing neuronal DNA damage, membrane protein impairment, and synaptic plasticity abnormalities—hallmarks of neurodegenerative diseases such as Alzheimer's disease.[3] These effects arise from the interplay of metabolic disorders, oxidative stress, and neurotransmitter disorders.[4] Especially, there is a significant population suffering from metabolic disorders, such as diabetes. They show heightened vulnerability due to hyperglycemic microenvironments that exacerbate cellular stress.[5] In such cases, the neurotoxic risk posed by MPs to patients with metabolic disorders is underestimated.

Accurate quantification of key biomarkers is fundamental to the assessment of pollutant-induced neurotoxicity. In particular, ROS (e.g., H_2O_2), neurotransmitters (e.g., acetylcholine, ACh), and metabolic indicators (e.g., glucose, Glu) are critical and well acknowledged for assessing oxidative stress, neurotoxic effects, and metabolic disorders.[6−8] Currently, considerable progress has been made in the detection of these biomarkers: H_2O_2 is typically detected via colorimetric, fluorescent, or chemiluminescent methods;[9−11] ACh is determined via ELISA-based colorimetric/fluorescent assays or GPCR-activation-based (GRAB) sensors;[12−14] and Glu is measured via glucometers or enzyme-linked reaction (ELR)-based colorimetric methods.[15] Although separate detection of these biomarkers is theoretically feasible, followed by

Received: October 14, 2025
Revised: January 8, 2026
Accepted: January 12, 2026
Published: January 23, 2026

https://doi.org/10.1021/envhealth.5c00556
Environ. Health 2026, 4, 1151−1161

comprehensive evaluation, current methods are limited by complex pretreatment and lengthy analysis. In addition, ROS and neurotransmitters are rapidly degraded by endogenous enzymes, and Glu levels also decrease over time. Compared with simultaneous detection techniques, separately measured biomarker concentration data cannot fully capture the correlations among oxidative stress, neurotransmitter disorders, and metabolic disorders, thereby constraining in-depth studies on the toxicological effects of pollutants, such as MPs.

Electrochemical sensing technologies, valued for their ease of miniaturization, high sensitivity, low detection limits, and real-time monitoring capability,[16] offer a promising approach to achieve the multidimensional assessment. Currently, modified electrodes based on natural enzymes, metal/metal oxide nanoparticles, or nanozymes have been widely used for detecting H_2O_2,[17] ACh,[18] and Glu.[19] While parallel sensor arrays based on such electrodes can detect multiple targets, they often suffer from interference between electrodes, complex signal processing, and structural constraints.[20,21] Employing similar synthesis and modification strategies for electrode-array fabrication can improve integration, streamline signal processing, reduce costs, and enhance performance, making these systems better suited for complex detection tasks and high-performance applications.

Currently, natural enzymes are widely employed for biomarker detection owing to their high specificity; however, their utility is constrained by intrinsic instability and active-site masking or structural distortion during immobilization.[22] To overcome these limitations, increasing attention has been directed toward nanozymes, which can serve as alternatives or synergistic complements to natural enzymes.[23,24] Nanozymes with peroxidase (POD)-like activity have been successfully applied for H_2O_2 sensing[25] and, when integrated with immobilized enzymes via loading or embedding, can enable cascade catalytic detection of analytes such as ACh and Glu.[18,19,26] If a capsule-shaped POD-like porous nanozyme is developed based on this concept for enzyme encapsulation and cascade catalysis, electrochemical detection of multiple targets can be achieved, which confers two major advantages: (i) from the nanozyme perspective, the materials exhibit broad environmental tolerance (wide pH range, high thermal stability, and resistance to proteolysis) and low production costs; and (ii) from the enzyme immobilization perspective, the capsule shell shields enzymes from environmental degradation, the porous architecture accelerates substrate diffusion, and the confined space allows greater conformational flexibility,[27] collectively enhancing cascade catalytic efficiency.[28] In addition, the enzyme@nanozyme nanocapsule cascade catalytic system possesses high methodological extensibility and structural isomorphism, enabling the flexible adaptation of the enzymes encapsulated within the nanozyme capsules according to the target analytes. This design affords substantial potential for future expansion toward quantitative detection of additional biomarkers.

In this study, metal-porphyrin-based covalent−organic framework (COF) materials were used as nanozymes and enzyme carriers to construct two cascade reactors by embedding different enzymes. Based on the nanozyme and cascade reactors, a three-channel multiplexed electrochemical sensing array was developed, enabling simultaneous detection of H_2O_2, ACh, and Glu in biological samples within 3 min without pretreatment, thereby reflecting the real-time concentration relationship among the three biomarkers. This sensor array was employed to multidimensionally assess the effects of different types, sizes, and aging degrees of MPs on neurons as well as their neurotoxic effects on neurons under hyperglycemia. Moreover, the investigation of the decreases in the concentrations of three biomarkers in biological samples after different resting times highlights the critical advantage of simultaneous and rapid detection in accurately evaluating the neurotoxicity of MPs. This work not only provides a novel detection platform for assessing the health risk of MPs but also offers robust technical support for elucidating the mechanisms underlying MP toxicity.

EXPERIMENTAL SECTION

Preparation of Enzyme@CoCOFNC

A 0.1 mol/L cobalt nitrate solution and a 1 mol/L 2-methylimidazole (2-MI) solution were separately prepared in H_2O. The solutions were mixed in a 2:8 volume ratio with vigorous stirring. The total volume was adjusted to 100 mL. After stirring for 10 min, the enzyme solution was added; the mixture was optimized to contain 30 mg of GOD or 5 mg of AChE plus 25 mg of CHO. The reaction proceeded for 20 min. The mixture was then centrifuged at 8500 rpm for 5 min, and the precipitate was collected. The precipitate was washed three times with water to remove excess metal ions, ligands, and loosely adsorbed enzymes. Finally, the precipitate was freeze-dried and labeled as Enzyme@ZIF-67. Pure ZIF-67 was synthesized by using the same method, excluding the enzyme addition step.

The synthesis of the COF nanocapsule was adapted from previous work.[29] First, Enzyme@ZIF-67 (20 mg) was dispersed in 12 mL of ethanol. 35 mg of 5,10,15,20-tetrakis(4-animophenyl)porphyrin (TAP) and 15 mg of thieno[3,2-*b*]thiophene-2,5-dicarboxaldehyde (TT) were dissolved in 8 mL of DMSO. A DMSO solution of $Sc(OTf)_3$ (6 g/L, 250 μL) was slowly added, followed by immediate sonication to ensure thorough dispersion. Stirring and sonication were alternated for 5 min each per cycle for a total reaction time of 30 min. After centrifugation at 5000 rpm for 5 min, the product was washed three times with DMSO and water, then freeze-dried, and labeled as Enzyme@ZIF-67@COF.

Enzyme@ZIF-67@COF (30 mg) was added to 15 mL of phosphate buffer solution (PBS) (50 mmol/L, pH 5) and allowed to stand for 4 h to remove the ZIF-67 template. After centrifugation at 5000 rpm for 5 min, the product was washed three times with water, then freeze-dried, and labeled as Enzyme@CoCOFNC (or En@CoCOFNC).

Aging of Polyethylene Terephthalate (PET)

60 mg of 100 nm PET particles was dispersed in 3 mL of seawater. Seawater was collected from Heishijiao Beach (Dalian, Liaoning Province, China) and filtered before use. The concentrations of major ions in seawater are listed in Table S1. The PET-seawater solution was placed in a transparent glass vial and exposed to UV light (38 W/m^2) under vigorous agitation to simulate sunlight and physical abrasion in the marine environment. After 48 h of aging, the PET was washed three times with water by centrifugation. The PET dispersion was adjusted to a concentration of 1 g/L. This material is referred to as PET-seawater (*PET aged in seawater*). Similarly, PET-water was prepared by dispersing PET in water.

Multiplexed Biosensor Validation in Biological Sample

The neuronal cells were centrifuged from the original culture medium. The cells were diluted to approximately 1.0×10^6 using the original culture medium and then lysed using a repeated freeze−thaw method. The sample was used for direct electrochemical testing without further pretreatment. Five sets of parallel experiments were conducted to ensure accuracy.

https://doi.org/10.1021/envhealth.5c00556
Environ. Health 2026, 4, 1151−1161

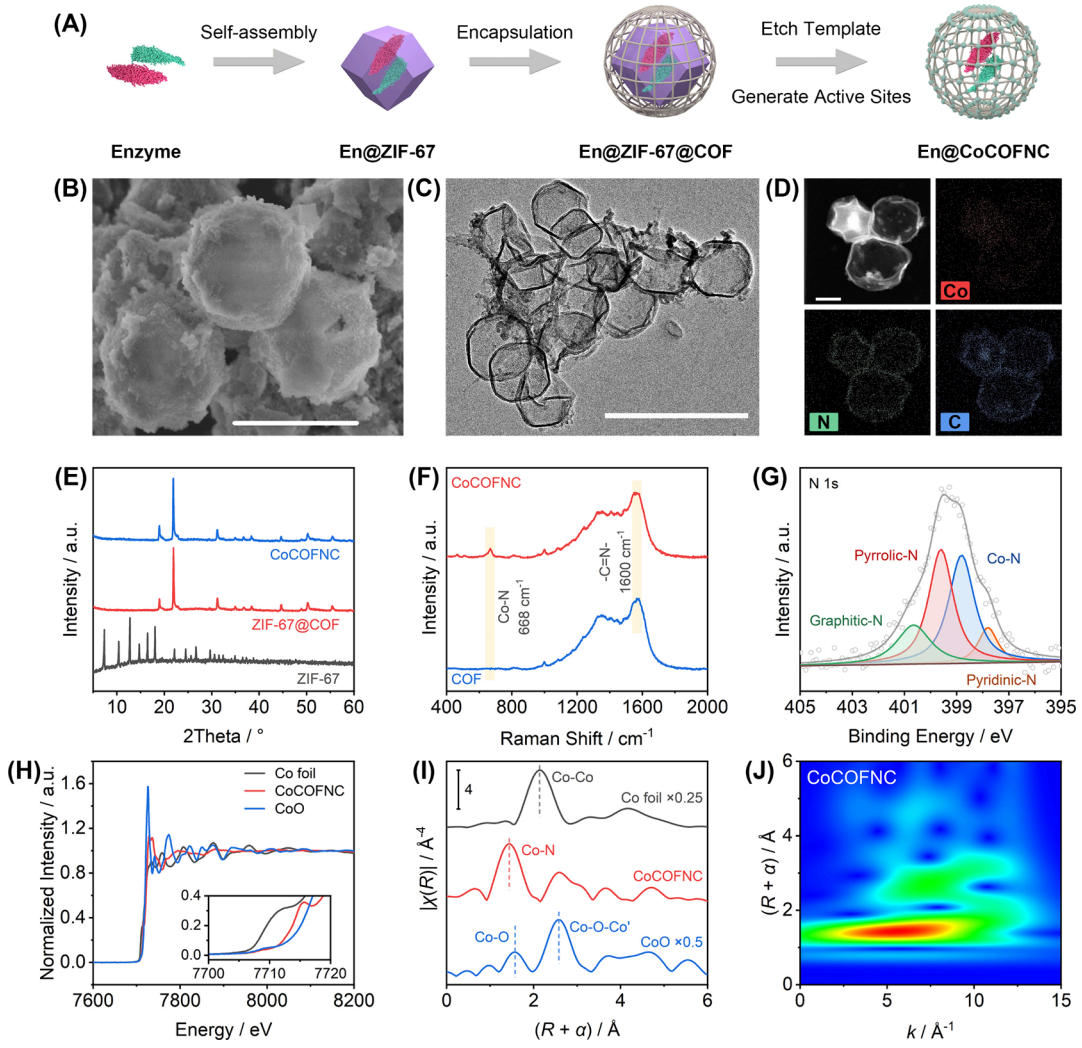

Figure 1. (A) Schematic illustration of the cobalt porphyrin-based COF nanocapsules (CoCOFNC); SEM (B), TEM (C), and EDS elemental mapping images (D) of CoCOFNC (showing the merged image and the dispersion of cobalt, nitrogen and carbon; scale bars of 200, 500, and 100 nm); (E) XRD patterns of ZIF-67, ZIF-67@COF, and CoCOFNC; (F) Raman spectra of COF and CoCOFNC; (G) N 1s XPS spectrum of CoCOFNC; Co K-edge XANES spectra (H) and k^3-weighted Fourier-transformed EXAFS spectra (I) for the Co K-edge of Co foil, CoO, and CoCOFNC; (J) k^3-weighted wavelet-transformed EXAFS spectrum of CoCOFNC.

RESULTS AND DISCUSSION

Synthesis and Characterization of CoCOFNC

The key principle in preparing metalloporphyrin-based COF nanocapsules is the sacrificial template method. A simplified flowchart of the preparation process is shown in Figure 1A. ZIF-67, the nanocapsule template, has a smooth-surfaced dodecahedral morphology; the ZIF-67@COF obtained by coating with porphyrin-based COF still retains a dodecahedral shape, but the shell layer slightly increases the particle size (Figure S1). SEM and TEM images (Figure 1B,C) show that the morphological features of hollow CoCOFNC nanocapsules tend to be spherical due to the selective dissolution of the ZIF-67 template with an average diameter of ~210 nm and a wall thickness of ~20 nm. Elemental mapping (Figure 1D) shows that CoCOFNC's main structure is composed of carbon with cobalt and nitrogen uniformly distributed across the surface. Benefiting from the combined contributions of the hollow structure and porous wall, the specific surface area of CoCOFNC was greatly increased to 1424.7 m^2/g compared to the precursors (Figure S2).

The XRD pattern (Figure 1E) confirms the successful synthesis of ZIF-67 with peaks at 2θ of 7.6°, 10.44°, 12.75°, and 18.13° corresponding to the (011), (002), (112), and (222) crystal planes, respectively.[30] These peaks are consistent with the simulated diffraction pattern of ZIF-67 (CCDC No. GITTOT02), indicating that ZIF-67 was successfully synthesized. Both ZIF-67@COF and CoCOFNC exhibit well-defined and distinguishable diffraction patterns (Figures 1E and S3). The peaks at 2θ = 3.6° and 7.4° correspond to the (100) and (200) crystal planes of the COF, while the peak near 22° corresponds to the (001) plane, indicating the presence of $\pi-\pi$ stacking.[31,32] According to Bragg's law, the interlayer spacing is ~4.0 Å. These results confirm the successful synthesis of the COF and its long-range ordered structure. FTIR and Raman spectra (Figures S4 and 1F) exhibit characteristic vibrations at 1650 cm^{-1} and 1600 cm^{-1}, respectively, indicating that the amino group and the aldehyde group of COF's ligands have condensed to form a Schiff base structure, thereby successfully forming the COF wall.[33,34]

The XPS survey spectrum (Figure S5) reveals that CoCOFNC mainly contains Co, N, and C, as well as small

https://doi.org/10.1021/envhealth.5c00556
Environ. Health 2026, 4, 1151−1161

amounts of S and O. The N 1s spectrum (Figure 1G) was deconvoluted into four nitrogen species: pyridinic-N (397.8 eV), pyrrolic-N (399.6 eV), Co−N (398.8 eV), and graphitic-N (400.7 eV),[35] indicating that Co coordinates with N to form a Co−N metalloporphyrin structure. The characteristic peak at 668 cm^{-1} in the Raman spectrum further corroborates the formation of the Co−N bond.[36] Figure 1H shows the K-edge X-ray absorption near-edge structure (XANES) spectra of Co in CoCOFNC, Co foil, and CoO. The results show that the absorption edge of CoCOFNC is close to that of CoO, suggesting a Co valence state of approximately +2. The Fourier transform of the extended X-ray absorption fine structure (FT-EXAFS) of CoCOFNC (Figure 1I) shows a main peak at ∼1.44 Å, primarily due to scattering from Co atoms to its first-shell N atoms. The wavelet-transformed EXAFS at Co K-edge further examines the coordination environment of Co in CoCOFNC. In contrast to Co foil and CoO (Figure S6), the contour plot of CoCOFNC (Figure 1J) shows a single intensity maximum at ∼5.85 $Å^{-1}$, attributed to Co−N coordination. Best-fit EXAFS analysis (Figure S7 and Table S2) reveals that each Co atom in CoCOFNC is coordinated with ∼4.10 N atoms, forming Co−N_4 bonds with an average bond length of ∼1.92 Å. The above results consistently indicate that Co^{2+} dissolved from the ZIF-67 template successfully embedded into the porphyrin cavity, forming stable Co−N_4 single atom sites.

Electrochemical Property of CoCOFNC and Catalytic Mechanism

To investigate the catalytic performance of the CoCOFNC nanozyme, electrochemical characterization was conducted on CoCOFNC-modified electrodes. The modified electrodes were tested using cyclic voltammetry (CV) and electrochemical impedance spectroscopy (EIS) tests in $Fe(CN)_6^{3-/4-}$ solution. The results (Figure 2A,B and Table S3) show that modifying the electrode with rGO increases the electrochemical active surface area (ECSA) and reduces the charge transfer resistance (R_{ct}) at the electrode interface, thereby compensating for the poor conductivity of COF. Next, the CV of the modified electrode in PBS containing H_2O_2 (Figure 2C) showed that CoCOFNC significantly enhanced both the oxidation peak current at +0.4 V and the reduction peak current at 0.0 V compared to pure rGO, demonstrating its excellent POD-like activity. The ratio of the oxidation peak current to the reduction peak current (I_{pa}/I_{pc}) was ∼0.57, indicating the irreversibility of this redox process. Since the enhancement of the reduction current signal was more significant, subsequent experiments on reaction mechanisms and quantitative analysis focused mainly on the reduction process. The rate-determining step of the H_2O_2 reduction reaction on the CoCOFNC/rGO/GCE surface was then studied. Varying the scan rate in the CV revealed that the logarithm of the scan rate was linearly related to the logarithm of the reduction current with a slope of approximately 0.503 (Figure 2D,E). This slope, close to 0.5, indicates that the rate-determining step of the reduction reaction is diffusion-controlled.[37] In addition, this nanozyme exhibited strong catalytic activity even at a pH of 7.4 (simulating the physiological conditions of human blood and tissue fluids; Text S1 and Figure 2F).

The structural validity of the Co−N_4 configuration was confirmed via the density functional theory (DFT). Moreover, the feasibility of two hypothetical reaction mechanisms was compared for various transition metal ions as active centers.

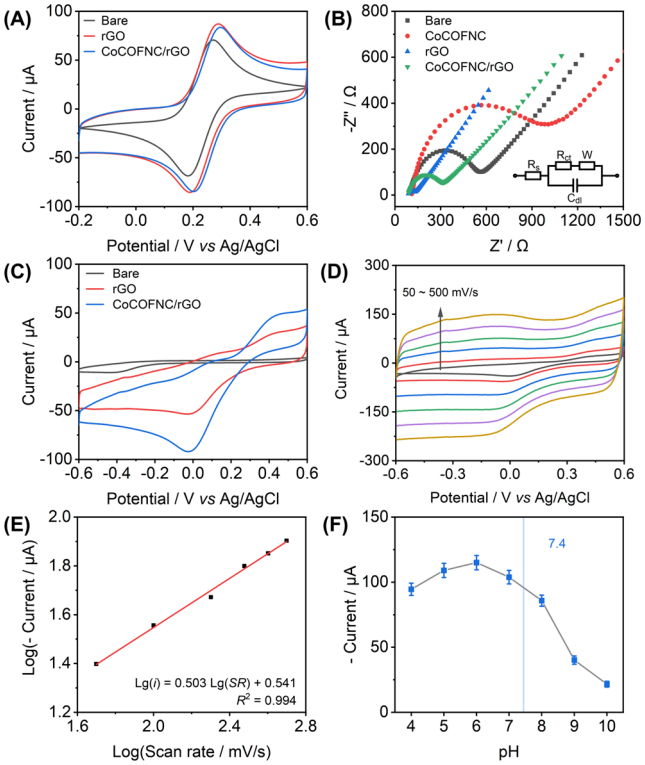

Figure 2. (A) CV curves obtained for different modified GCEs in 5 mmol/L of $Fe(CN)_6^{3-/4-}$ (1:1) in 0.1 mol/L KCl solution; (B) Nyquist diagrams obtained for different modified GCEs in 5 mmol/L of $Fe(CN)_6^{3-/4-}$ (1:1) in 0.1 mol/L KCl solution (inset: the artificial circuit of the EIS system); (C) CV curves obtained for bare GCE, rGO/RCE, and CoCOFNC/rGO/GCE in 5 mmol/L of H_2O_2 in PBS (pH 7.4, 50 mmol/L); (D) CV curves recorded for CoCOFNC/rGO/GCE in 5 mmol/L of H_2O_2 in PBS (pH 7.4, 50 mmol/L) at different scan rates from 50 to 500 mV/s; (E) Randles-Sevcik plot of Log(Reduced peak current) vs Log(Scan rate); (F) plot of the reduction current of H_2O_2 measured by CoCOFNC/rGO/GCE via CV vs the pH (4−10) of PBS.

Detailed calculation results and related discussions are provided in Text S2. The results demonstrated that Co and Fe exhibit excellent catalytic activity, consistent with the experimental findings. However, the synthesis conditions for Fe-based MOFs typically require high temperatures or long synthesis times, which are not conducive to preserving the activity of the encapsulated enzymes. Therefore, this study selected Co^{2+} instead of an iron ion as the metal source in the MOF sacrificial template due to its relatively mild synthesis conditions.

Encapsulation of Enzymes by CoCOFNC

To achieve specific recognition and quantitative detection of acetylcholine and Glu, two enzyme-nanozyme cascade reactors were constructed by encapsulating AChE-CHO or GOD in CoCOFNC, respectively. These targets generate H_2O_2 under the catalysis of enzymes, which is further degraded under the catalysis of POD-like nanozymes while producing electrochemical signals, thereby enabling quantitative detection of these targets. The morphology of Enzymes@CoCOFNC was characterized (Figure 3Ai), and it had a hollow spherical structure like CoCOFNC. Subsequently, GOD, AChE, and CHO were labeled with different dyes (e.g., FITC and RhB) before material synthesis. Laser confocal microscopy images (Figure 3A,B) confirmed that, in the constructed enzyme-

https://doi.org/10.1021/envhealth.5c00556
Environ. Health 2026, 4, 1151−1161

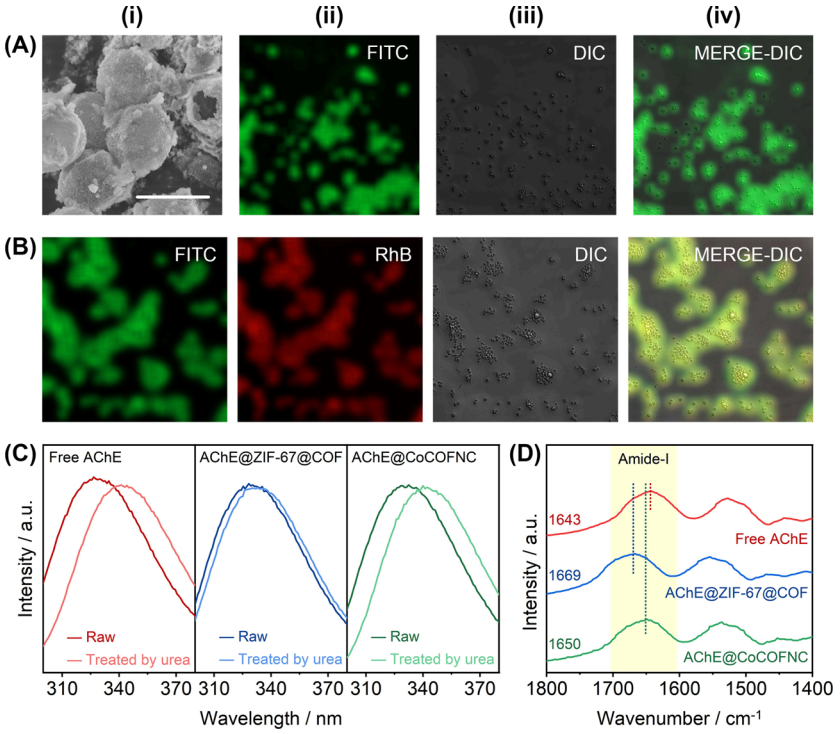

Figure 3. (Ai) SEM of GOD@CoCOFNC (Scale bar = 200 nm); (Aii to Aiv) CLSM image, DIC image, and overlaid CLSM image of FITC-GOD@CoCOFNC; (Bi to Biv) CLSM images (FITC and RhB), DIC image, and overlaid CLSM image of FITC-AChE+RhB-CHO@CoCOFNC; (C) fluorescence spectra of free AChE, AChE@ZIF-67@COF, and AChE@COCOFNC in Tris buffer (pH 7.4, 50 mmol/L) before and after exposure to 8 mol/L urea, respectively; (D) IR spectra of free AChE, AChE@ZIF-67@COF, and AChE@COCOFNC.

nanozyme cascade systems (GOD@CoCOFNC and AChE +CHO@CoCOFNC), these enzymes were successfully encapsulated within the CoCOFNC nanocapsules. The enzyme loading of AChE and CHO in AChE+CHO@CoCOFNC was 1.6 and 7.6 wt %, respectively, with encapsulation efficiencies of 65.7% and 88.6%. In GOD@CoCOFNC, the enzyme loading of GOD was 4.4 wt % and the encapsulation efficiency was 73.6%.

The hollow structure of the COF nanozyme capsules can better preserve the conformational freedom of encapsulated enzymes. This was confirmed by fluorescence spectroscopy (Figure 3C and Text S3), where the fluorescence spectrum of AChE encapsulated within the nanozyme capsules exhibited a redshift similar to that of free AChE, indicating that it has a high degree of conformational freedom, comparable to that of free enzymes.[38] Infrared spectroscopy (IR) further supported this observation (Figure 3D and Text S3), revealing minimal differences in vibrational frequencies between AChE@CoCOFNC and free AChE. This result also indicates that CoCOFNC imposes minimal conformational constraints on the enzyme, thereby favoring the retention of enzymatic activity.[39] In contrast, the encapsulation of enzymes within MOFs or COFs often restricts their conformational freedom, leading to reduced or even abolished enzymatic activity.[27]

Then, the catalytic activities of the free enzymes and the enzyme-loaded materials were evaluated, and the corresponding kinetic parameters were calculated. The results are presented in Figure S8 and Table S4. Compared with the free enzymes, the V_{max} values of the enzymes encapsulated in ZIF-67 and ZIF-67@COF decreased substantially, while their K_m values increased, indicating reduced catalytic efficiency and diminished substrate affinity. After removal of the sacrificial template, both V_{max} and K_m exhibited significant recovery, approaching the levels observed for the free enzymes, demonstrating that the CoCOFNC nanocapsule is more favorable for preserving enzymatic activity. Combined with the conclusions in Figure 3C,D, these findings further indicate that enzymes encapsulated within the CoCOFNC nanocapsules possess greater conformational freedom and consequently display catalytic efficiency and substrate affinity more comparable to those of the free enzymes.

Subsequently, electrochemical characterization of the two enzyme@nanozyme-modified electrodes revealed that their R_{ct} was slightly higher than that of CoCOFNC/rGO/GCE (Figure S9 and Table S3). This observation can be attributed to the inherently low electrical conductivity of enzymes (proteins), which may increase the electrode impedance upon their addition and modification. Furthermore, CV testing in $Fe(CN)_6^{3-/4-}$ solution showed no significant differences in ECSA among the three modified electrodes (Figure S10), further supporting that enzyme addition exerts negligible influence on the electrochemical properties of the electrode interface.

Sensing Performance of CoCOFNC-Based Modified Electrodes

Under optimal modified electrode preparation conditions, the ability of the three modified electrodes to detect H_2O_2, ACh, and Glu was evaluated by differential pulse voltammetry (DPV) (Figures 4A–C and S11). The results indicate that the reduction peak current of H_2O_2 has a linear relationship with its concentration in the range of 0.5 μmol/L to 8.4 mmol/L with the linear equation $i/\mu A = 15.2 \times c/\text{mmol/L} + 3.34$ (R^2 = 0.999). The limit of detection (LOD) was determined to be 9 nmol/L (S/N = 3), which is lower than the H_2O_2 concentration reported in healthy cells without oxidative

https://doi.org/10.1021/envhealth.5c00556
Environ. Health 2026, 4, 1151−1161

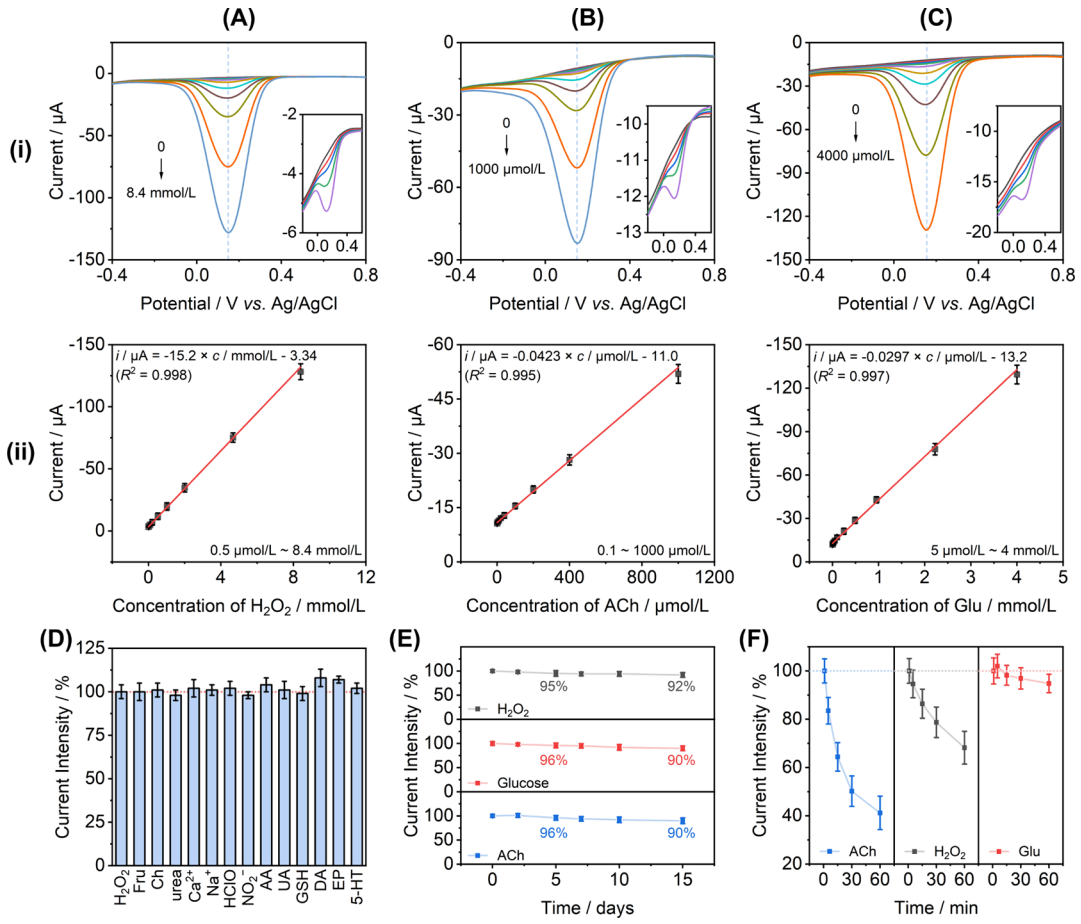

Figure 4. DPV curves (i) and corresponding calibration curves (ii) for different concentrations of H_2O_2 (A), ACh (B), and Glu (C) in PBS (pH 7.4, 50 mmol/L) by CoCOFNC/rGO/GCE, AChE+CHO@CoCOFNC/rGO/GCE, and GOD@CoCOFNC/rGO/GCE, respectively; (D) selectivity of CoCOFNC/rGO/SPE for H_2O_2 detection in the presence of 1 μmol/L H_2O_2 with and without the interfering substances at supraphysiological concentrations in PBS (pH 7.4, 50 mmol/L); (E) the long-term stability of CoCOFNC/rGO/GCE, AChE+CHO@CoCOFNC/rGO/GCE, and GOD@CoCOFNC/rGO/GCE; (F) the current intensities of biomarkers measured by modified electrode after leaving the neuronal lysate at room temperature for different periods of time.

stress.[40] For AChE+CHO@CoCOFNC/rGO/GCE, ACh showed a linear relationship with the reduction peak current in the concentration range of 0.1 μmol/L to 1000 μmol/L with the linear equation $i/\mu A = 0.0423 \times c/\mu mol/L + 11.0$ (R^2 = 0.997) and the LOD of 18 nmol/L (S/N = 3). For GOD@CoCOFNC/rGO/GCE, Glu exhibited a linear relationship with the reduction peak current in the concentration range of 5 μmol/L to 4 mmol/L with the linear equation $i/\mu A = 0.0297 \times c/\mu mol/L + 13.2$ (R^2 = 0.997) and the LOD of 2.2 μmol/L (S/N = 3). The concentration of ACh in the serum of healthy individuals ranges from 0.2 to 1.3 μmol/L;[41] the Glu concentration in typical neural cell culture environments is in the mmol/L range.[42] The LODs of the three sensors are below the application threshold, meeting the detection requirements for real samples. Furthermore, compared with current reports on electrochemical detection of H_2O_2, ACh, and Glu, all three modified electrodes exhibited superior detection performance (Tables S5 to S7).

Given the high specific recognition capabilities of AChE, CHO, and GOD, the specificity of the CoCOFNC nanozyme toward H_2O_2 becomes the key to achieving accurate target identification in the cascade catalytic system. Herein, the selectivity of CoCOFNC/rGO/SPE was investigated. Several common coexisting substances, other reactive species, and structural analogs that may interfere in the detection environment were selected, including urea, fructose (Fru), choline (Ch), ascorbic acid (AA), uric acid (UA), glutathione (GSH), dopamine (DA), epinephrine (EP), serotonin (5-HT), HClO, NO_2^-, Na^+, and Ca^{2+}. These substances at supraphysiological concentrations were mixed with 1 μmol/L H_2O_2 (Table S8) and tested by DPV (Figure S12). Figure 4D shows that the quantitative detection error of H_2O_2 is less than 8% under the impact of interfering substances, indicating that this modified electrode has a good selectivity for H_2O_2.

To enhance the portability of the sensing array while reducing the manufacturing cost, a three-channel multiplexed electrochemical sensing array based on screen-printed electrodes (SPE) was fabricated, and the detection performance was comparable to that of modified GCEs. Working curves were calibrated within the rational concentration ranges of these three targets in biological samples to meet the detection requirements for real samples (Figure S13): the working curve for H_2O_2 in the range of 0−1000 nmol/L was $i/\mu A = -9.37 \times c/\mu mol/L - 6.72$ (R^2 = 0.998) with an LOD of 13 nmol/L; the working curve for ACh in the range of 0−1 μmol/L was $i/\mu A = -3.67 \times c/\mu mol/L - 6.62$ (R^2 = 0.994) with an LOD of 22 nmol/L; the working curve for Glu in the range of 0−4

https://doi.org/10.1021/envhealth.5c00556
Environ. Health 2026, 4, 1151−1161

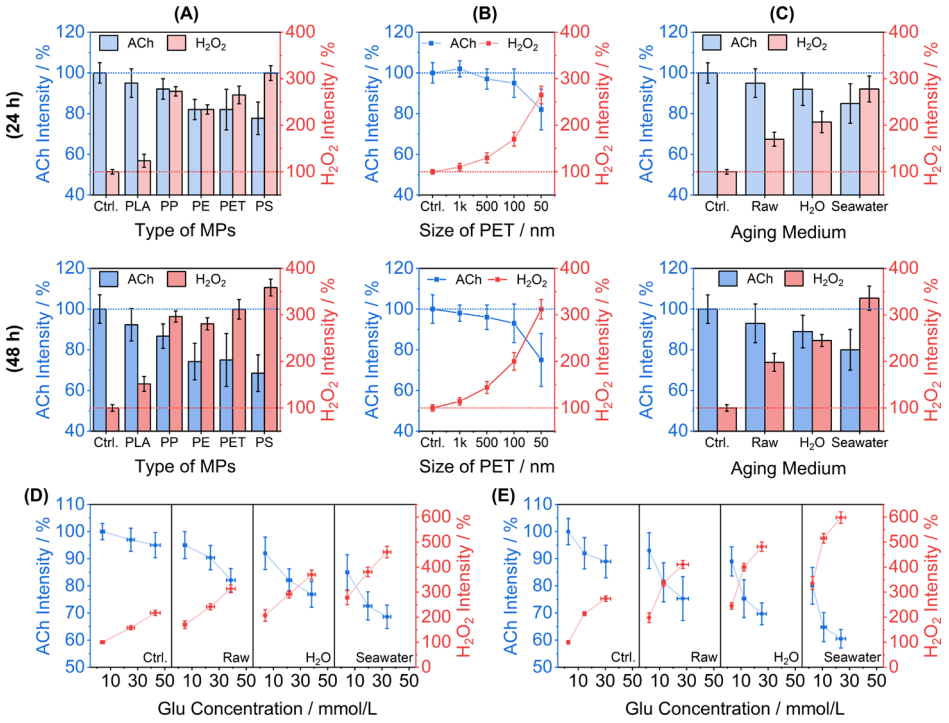

Figure 5. Levels of ACh and H_2O_2 in the cell lysates induced by the MPs with different types (A), sizes (B), and aging degrees (C); levels of H_2O_2 and ACh in the cell lysates coinduced by different concentrations of Glu and PET with different aging degrees (incubation of 24 h (D) and 48 h (E)).

mmol/L was $i/\mu A = -0.0357 \times c/\mu mol/L - 3.42$ ($R^2 = 0.999$) with an LOD of 1.0 μmol/L.

To assess the electrodes' capability to detect these three biomarkers in real samples, spiked recovery tests were performed using cell culture medium and horse serum. The tests were conducted at low, medium, and high concentrations within the sensor's detection range for comprehensive validation. The results (Tables S9–S11) indicate that the overall recovery rates for H_2O_2, ACh, and Glu range from 97% to 105%, 103% to 106%, and 98% to 107%, respectively. Meanwhile, a comparison with methods commonly used in biochemical analysis revealed that the sensing array exhibits detection performance comparable to that of those methods. These findings suggest that the biosensors exhibit excellent capability for detecting complex biological samples.

The repeatability, reproducibility, and storage stability of three types of modified electrodes (including CoCOFNC/rGO/GCE, AChE+CHO@CoCOFNC/rGO/GCE, and GOD@CoCOFNC/rGO/GCE) were evaluated to ensure their reliability for real-sample analysis. Ten independently fabricated batches of modified electrodes were prepared using the same protocol, and each electrode was subjected to five parallel measurements of their electrochemical responses toward their analytes (500 nmol/L H_2O_2; 500 nmol/L ACh; and 1 mmol/L Glu, respectively) to assess their stability. As illustrated in Figure S14, the relative standard deviations (RSDs) of repeated measurements for a single electrode remained below 5.1%, 4.8%, and 4.6%, respectively, indicating good repeatability of the modified electrodes. Meanwhile, the interelectrode RSDs among the ten electrodes were 2.4%, 3.2%, and 2.7%, respectively, demonstrating good reproducibility of the electrodes. As shown in Figure 4E, the electrochemical responses of the sensing array to all three analytes remained above 95% of the initial responses after storage at 4 °C for 5 days; even after 15 days of storage, considerable electrochemical responses were still maintained. This indicates that this POD-like nanozyme possesses good stability. Meanwhile, the nanozyme capsules effectively protected the encapsulated enzyme activity. These results demonstrate that the fabricated modified electrodes possess long storage lifetimes and excellent precision, making them suitable for the detection of real samples.

The greenness of the sensing array was analyzed using AGREE software and compared with other common analytical methods for these targets,[43] taking the spectrophotometric method and the ultraperformance liquid chromatography-tandem mass spectrometry (UPLC-MS/MS) method as examples. AGREE, based on the 12 principles of green analytical chemistry, provides a visual assessment through a color pictogram ranging from 0 to 1, where a higher value indicates a more environmentally friendly choice.[44] The detailed calculation process is shown in Text S4, and the calculation results are presented in Figure S15. The sensing array for the three targets scored 0.76; the spectrophotometric method scored 0.59, and the UPLC-MS/MS method scored 0.38. These results demonstrate that the sensing array has strong sustainability and environmental friendliness. It is worth noting that the sensing array performs well in terms of "sample treatment", "device positioning", "sample preparation stages", and "automation, miniaturization". It particularly excels in "analysis throughput", achieving simultaneous detection of three analytes and 20 rounds of tests per hour (i.e., one test can be completed in 3 min). This performance is highly critical and beneficial for the immediate detection of ROS and neurotransmitters with a short half-life.

At present, reports on technologies capable of simultaneously detecting these targets remain relatively scarce. Existing studies typically employ multiple methods with

https://doi.org/10.1021/envhealth.5c00556
Environ. Health 2026, 4, 1151−1161

complex pretreatment and time-consuming detection processes to detect different targets separately, including spectrophotometry, chromatography, and mass spectrometry. This makes simultaneous detection difficult to achieve. In this study, quantitative analyses of cell lysates stored at room temperature for varying durations revealed that the concentrations of these targets decreased with an increase in storage time (Figure 4F). Among them, after 60 min, ACh levels declined most rapidly with the current signal reduced to only 41.2% of the initial value; H_2O_2 also decreased, retaining just 78.2% of its initial level. Meanwhile, Glu was comparatively stable but still dropped to 94.8%. This phenomenon is primarily attributed to the rapid degradation of active substances in biological samples by endogenous enzymes.[45] To overcome this problem, enzyme inhibitors are commonly used to reduce the activity of relevant enzymes in the sample in order to preserve the analyte as much as possible.[46] However, this greatly tests the operational skills of the experimenters. It can be seen that detection time exerts a significant influence on experimental outcomes: delayed measurements lead to an underestimation of target concentrations and confound assessments of the concentration relationship between different targets, thereby failing to accurately reflect the true metabolic state of the sample. Thus, the electrochemical sensing array, which enables rapid detection of the three targets without additional pretreatment, demonstrated remarkable advantages. Importantly, this sensing array operates under a highly unified detection principle: to detect H_2O_2 existing in the system or produced in the cascade reaction based on POD-like CoCOFNC nanozyme. Consequently, each channel of the sensing array can operate using similar electrochemical parameters. Unlike a simple array formed by paralleling three independent working electrodes based on different detection mechanisms, such uniformity significantly reduces cross-interference among multiple electrode channels while simplifying the design of portable potentiometry, thereby further enhancing its practical applicability.[20,21]

Multidimensional Assessment of the Impact of MPs on Neurons

Based on this sensing array, we investigated the effects of various MPs or Glu levels in culture medium on the production of ACh and H_2O_2 in neuronal cells. In this study, five common types of MPs (particle size of 50 nm) were selected, including poly(lactic acid) (PLA), polypropylene (PP), polyethylene (PE), polyethylene terephthalate (PET), and polystyrene (PS). The results (Figure 5A) demonstrated that most MPs stimulated neurons to release greater amounts of H_2O_2 with the intensity following the order: PS > PET ≈ PP > PE > PLA, while the inhibitory effects on ACh synthesis were ranked as PS > PET ≈ PE > PP > PLA. The two trends are not precisely the same, especially PE and PP, indicating that different types of MPs cause a varying degree of neurotoxic effects, which may be attributed to differences in their toxic mechanisms.[47] Specifically, compared with PE, PP exhibited a stronger stimulatory effect on H_2O_2 production but a weaker inhibitory effect on ACh synthesis. PP induced only a significant ACh inhibitory effect ($p < 0.05$) with an inhibition rate of 92.1%, whereas PE showed a highly significant ACh inhibitory effect ($p < 0.01$) with an inhibition rate of 82%. However, ACh and H_2O_2 rapidly degrade after sample preparation (Figure 4F). Particularly within the initial 15 min, ACh showed the fastest degradation, dropping to 64.4% of its initial concentration, while the H_2O_2 concentration decreased to 85.4%. If traditional detection techniques are used (with testing procedures generally taking more than 15 min), such rapid degradation could introduce substantial quantitative errors, whose impact could obscure the concentration changes of biomarkers induced by MPs, making it difficult to distinguish differences in toxic effects among varying MPs. Meanwhile, from a temporal perspective, compared with 24 h of incubation with MPs, after 48 h of incubation, the concentration of H_2O_2 increased significantly, whereas ACh slightly decreased under the influence of PE, PET, and PS. The errors caused by endogenous degradation could amplify the inhibitory effect on ACh and underestimate the promoting effect on H_2O_2. Notably, this sensing array enables simultaneous and rapid detection of these biomarkers, thereby minimizing the impact of degradation and ensuring the more precise quantification of biomarkers.

The toxic effects of MPs exhibited a clear size-dependent relationship (Figure 5B). Within the size range of 50−1000 nm, smaller PET particles exerted more pronounced effects in stimulating H_2O_2 release and inhibiting ACh synthesis in neurons with a negative correlation observed between these two responses. This phenomenon may be attributed to the stronger oxidative stress induced by smaller MPs, which leads to elevated levels of H_2O_2 expression, while simultaneously causing greater cellular dysfunction, thereby reducing ACh levels.[48] If the degradation of the biomarkers in the samples is not considered during measurement, it may lead to an underestimation of the actual concentrations of ACh and H_2O_2, thereby misjudging the toxic effect of MPs on the neurons.

Similarly, the advantage of timely detection with the sensing array is also evident in analyzing the toxic effects of aged MPs. In this context, PET, one of the most common MPs in the ocean, was selected as a model, and the related aged MP samples were prepared by simulating sunlight exposure and physical abrasion in both pure water and seawater, followed by thorough characterization (Text S5). The results (Figure 5C) revealed that the extent of H_2O_2 elevation induced by different aged MPs followed the order: PET-seawater > PET-water ≈ PET. In terms of the inhibitory effect on ACh synthesis, the order was PET-seawater > PET-water > PET. Aged MPs, especially those aged in actual environments, exhibit stronger toxic effects due to their higher content of oxygen-containing functional groups and their carrier effect on pollutants, which is consistent with the conclusions reported in previous literature.[49] Moreover, with prolonged incubation, the variation in ACh was minimal, whereas H_2O_2 exhibited a marked increase. This could be attributed to the different aging processes, which result in distinct mechanisms of toxic effects. Meanwhile, the capture of this subtle difference further confirmed the advantage of the sensing array in simultaneously and rapidly detecting the analytes.

Finally, the sensing array was employed to investigate the combined toxicity of aged MPs under hyperglycemia as well as to preliminarily explore the concentration correlation among the three biomarkers. After neurons were exposed to Raw PET, PET-water, and PET-seawater for 24 and 48 h, their metabolic alterations are shown in Figures 5D,E and S16. All three types of MPs induced varying degrees of toxic effects. In the control group, as the Glu concentration in the medium increased from 10 to 50 mmol/L, ACh showed only a slight decrease, while H_2O_2 exhibited a modest increase. However, in the MP-treated

https://doi.org/10.1021/envhealth.5c00556
Environ. Health 2026, 4, 1151−1161

groups, particularly those after aging, this trend was markedly amplified. Among them, MPs aged in seawater exhibited the strongest toxicity and significantly enhanced glucose uptake. With the incubation prolonged to 48 h, the decline in ACh became more pronounced, while the increase in H_2O_2 was more drastic, indicating a clear time-dependent cumulative effect. These changes reflect the disruption of neuronal function and metabolism by MPs under hyperglycemic conditions. This can be attributed to the complex toxicological mechanisms of MPs and hyperglycemia:[8,50−52] Hyperglycemic conditions lead to metabolic abnormalities in neurons, resulting in a surge of ROS. MPs further intensify oxidative stress, leading to additional H_2O_2 production. Excessive H_2O_2 can oxidize the active site of choline acetyltransferase while simultaneously promoting tyrosine phosphorylation of AChE, thereby inhibiting ACh synthesis and accelerating it hydrolysis. This substantial reduction in ACh levels can impair synaptic transmission, induce abnormal energy demands in neurons, and trigger compensatory Glu uptake, leading to a vicious cycle. It is worth emphasizing that the detection of subtle concentration changes among these biomarkers relies on the multiplexed electrochemical sensor developed in this study. Unlike conventional methods that measure biomarkers individually, this sensor enables the simultaneous and rapid quantification of ACh, H_2O_2, and Glu within the same time window. This not only avoids signal attenuation caused by the short half-lives of active species but also minimizes errors arising from batch-to-batch variations. Such advantages facilitate the establishment of correlations among different biomarkers and provide new insights into the effects of the Glu concentration, MP, and exposure duration on neuronal metabolism.

CONCLUSIONS

Multidimensional biomarker analysis is crucial for understanding the correlations among metabolic disorders, oxidative stress, and neurotransmitter disorders, as well as for evaluating the neurotoxic effects of pollutants. To meet this need, we propose a highly extensible enzyme-nanozyme cascade strategy and construct a multiplexed electrochemical biosensor array for the simultaneous detection of H_2O_2, ACh, and Glu. In the design of the array, nanozyme capsules not only protect the conformational freedom and catalytic activity of encapsulated enzymes but also serve as an essential part of the cascade reaction to achieve specific recognition of the analytes. Moreover, this synthetic approach is compatible with a variety of biomarkers whose enzymatic reactions generate H_2O_2 as a byproduct, demonstrating a high degree of extensibility. The three channels of the array are prepared through similar processes and maintain a highly unified working mechanism. This isomorphic design significantly reduces the mutual interference between channels, simplifies the circuit and algorithm design of the portable potentiometry, and thereby enhances the overall performance of the array. In its detection performance, the array exhibits a wide detection range, low LOD, high selectivity, and strong anti-interference ability for three analytes. Of particular importance is that it requires no additional pretreatment and is capable of simultaneously and accurately quantifying these short half-life, easily degradable analytes in real biological samples within 3 min, minimizing measurement errors caused by detection delays and thereby facilitating the elucidation of their concentration correlations. With this sensor, the neurotoxic effects induced by various MPs on neurons were systematically and multidimensionally evaluated, and it was confirmed that hyperglycemia significantly influence the neurotoxic effects of MP. In summary, this study provides effective technical support for advancing investigations into pollutant-induced neurotoxicity and related health risks.

Building on these outcomes, the multiplexed sensor demonstrated considerable potential for biomedical and public health applications. The sensor exhibits robust analytical performance in complex matrices, enabling rapid and accurate detection of diverse sample types, such as neuronal lysates, serum, and cell culture media. With the continued development of noninvasive sampling strategies, together with ongoing advances in natural enzyme resources and enzyme engineering technologies, such integrated systems could facilitate chronic monitoring of neurochemical microenvironments, thereby supporting disease management, therapeutic assessment, and population-level health surveillance.

ASSOCIATED CONTENT

Supporting Information

The Supporting Information is available free of charge at https://pubs.acs.org/doi/10.1021/envhealth.5c00556.

Detailed materials, instruments, and experimental methods; characterization and electrochemical performance results of En@CoCOFNC; proposed reaction mechanism and DFT calculation results; characterization of MPs and MTT assay results (PDF)

AUTHOR INFORMATION

Corresponding Author

Huimin Zhao − *Key Laboratory of Industrial Ecology and Environmental Engineering (Ministry of Education, China), Dalian University of Technology, Dalian 116024, China;* orcid.org/0000-0001-8952-801X; Email: zhaohuim@dlut.edu.cn

Authors

Yifei Xing − *Key Laboratory of Industrial Ecology and Environmental Engineering (Ministry of Education, China), Dalian University of Technology, Dalian 116024, China*

Xuehan Wei − *Key Laboratory of Industrial Ecology and Environmental Engineering (Ministry of Education, China), Dalian University of Technology, Dalian 116024, China*

Xu Liang − *Key Laboratory of Bio-Intelligent Manufacturing, School of Bioengineering (Ministry of Education, China), Dalian University of Technology, Dalian, Liaoning 116000, China*

Complete contact information is available at: https://pubs.acs.org/10.1021/envhealth.5c00556

Author Contributions

Yifei Xing: Writing−original draft, Conceptualization. **Xuehan Wei**: Writing−original draft, Methodology, Investigation. **Xu Liang**: Investigation, Data curation. **Huimin Zhao**: Writing−review and editing, Supervision, Resources, Project administration, Methodology, Investigation, Funding acquisition, Data curation, Conceptualization.

Notes

The authors declare no competing financial interest.

https://doi.org/10.1021/envhealth.5c00556
Environ. Health 2026, 4, 1151−1161

■ ACKNOWLEDGMENTS

This work is supported by the Natural Science Foundation of China (No.21976022) and the Dalian POCT laboratory. The authors acknowledge the assistance of the Instrumental Analysis Center of Dalian University of Technology.

■ REFERENCES

(1) Chen, Z.; Elektorowicz, M.; An, C.; Tian, X.; Wang, Z.; Yang, X.; Lyu, L. Revealing the Freezing-Induced Alteration in Microplastic Behavior and Its Implication for the Microplastics Released from Seasonal Ice. *Environ. Sci. Technol.* **2024**, *58* (30), 13529−13539.

(2) Ding, R.; Dong, Y.; Ouyang, Z.; Zuo, X.; Zhang, Y.; Guo, X. Reducing uncertainty and confronting ignorance about the potential impacts of microplastic on animals: A critical review. *TrAC Trends Anal. Chem.* **2024**, *171*, 117484.

(3) Li, P.; Liu, J. Micro(nano)plastics in the Human Body: Sources, Occurrences, Fates, and Health Risks. *Environ. Sci. Technol.* **2024**, *58* (7), 3065−3078.

(4) Paul, I.; Mondal, P.; Haldar, D.; Halder, G. Beyond the cradle - Amidst microplastics and the ongoing peril during pregnancy and neonatal stages: A holistic review. *J. Hazard. Mater.* **2024**, *469*, 133963.

(5) Parasin, N.; Amnuaylojaroen, T.; Saokaew, S.; Sittichai, N.; Tabkhan, N.; Dilokthornsakul, P. Outdoor air pollution exposure and the risk of type 2 diabetes mellitus: A systematic umbrella review and meta-analysis. *Environ. Res.* **2025**, *269*, 120885.

(6) Pokhrel, S.; Heo, G.; Mathews, I.; Yokoi, S.; Matsui, T.; Mitsutake, A.; Wakatsuki, S.; Mochly-Rosen, D. A hidden cysteine in Fis1 targeted to prevent excessive mitochondrial fission and dysfunction under oxidative stress. *Nat. Commun.* **2025**, *16* (1), 4187.

(7) Hernández, A. F.; Lacasaña, M.; Garcia-Cortés, H.; Fernández, M. F.; Gozález-Alzaga, B. Identification and prioritisation of biomarkers of organophosphorus compounds-induced neurotoxicity. *Environ. Int.* **2025**, *199*, 109446.

(8) Tomlinson, D. R.; Gardiner, N. J. Glucose neurotoxicity. *Nat. Rev. Neurosci.* **2008**, *9* (1), 36−45.

(9) Mu, X.; Wang, J.; He, H.; Li, Q.; Yang, B.; Wang, J.; Liu, H.; Gao, Y.; Ouyang, L.; Sun, S.; Ren, Q.; Shi, X.; Hao, W.; Fei, Q.; Yang, J.; Li, L.; Vest, R.; Wyss-Coray, T.; Luo, J.; Zhang, X. An oligomeric semiconducting nanozyme with ultrafast electron transfers alleviates acute brain injury. *Sci. Adv.* **2021**, *7* (46), No. eabk1210.

(10) Li, C.; Wu, Y.; Chen, Q.; Luo, Y.; Liu, P.; Zhou, Z.; Zhao, Z.; Zhang, T.; Su, B.; Sun, T.; Jiang, C. Pleiotropic Microenvironment Remodeling Micelles for Cerebral Ischemia-Reperfusion Injury Therapy by Inhibiting Neuronal Ferroptosis and Glial Overactivation. *ACS Nano* **2023**, *17* (18), 18164−18177.

(11) Ye, S.; Hananya, N.; Green, O.; Chen, H.; Zhao, A. Q.; Shen, J.; Shabat, D.; Yang, D. A Highly Selective and Sensitive Chemiluminescent Probe for Real-Time Monitoring of Hydrogen Peroxide in Cells and Animals. *Angew. Chem.-Int. Ed.* **2020**, *59* (34), 14326−14330.

(12) Ding, P.; Han, Y.; Sun, Y.; Chen, X.; Ge, Q.; Huang, W.; Zhang, L.; Li, A. J.; Hu, G.; Yu, Y. Synergistic neurotoxicity of clothianidin and photoaged microplastics in zebrafish: Implications for neuroendocrine disruption. *Environ. Pollut.* **2025**, *368*, 125797.

(13) Nguyen, X. T. A.; Le, T. N. U.; Nguyen, T. Q.; Thi Thuy Ha, H.; Artati, A.; Leong, N. C. P.; Nguyen, D. T.; Lim, P. Y.; Susanto, A. V.; Huang, Q.; Fam, L.; Leong, L. N.; Bonne, I.; Lee, A.; Granadillo, J. L.; Gooch, C.; Yu, D.; Huang, H.; Soong, T. W.; Chang, M. W.; Wenk, M. R.; Adamski, J.; Cazenave-Gassiot, A.; Nguyen, L. N. MFSD7c functions as a transporter of choline at the blood-brain barrier. *Cell Res.* **2024**, *34* (3), 245−257.

(14) Xia, X.; Li, Y. A high-performance GRAB sensor reveals differences in the dynamics and molecular regulation between neuropeptide and neurotransmitter release. *Nat. Commun.* **2025**, *16* (1), 819.

(15) van der Kooij, M. A.; Jene, T.; Treccani, G.; Miederer, I.; Hasch, A.; Voelxen, N.; Walenta, S.; Müller, M. B. Chronic social stress-induced hyperglycemia in mice couples individual stress susceptibility to impaired spatial memory. *Proc. Natl. Acad. Sci. U. S. A.* **2018**, *115* (43), No. E10187-E10196.

(16) Wu, L.; Yang, F.; Niu, K.; Zhao, J.; Zhang, X.; Lu, X.; Li, X.; Huang, Y.; Chen, J. Single-Mg-Atom Catalyst with a Dual Active Center as an Emerging Promising Sensing Platform. *ACS Appl. Mater. Interfaces.* **2024**, *16* (16), 20959−20968.

(17) Zhao, S.; Zang, G.; Zhang, Y.; Liu, H.; Wang, N.; Cai, S.; Durkan, C.; Xie, G.; Wang, G. Recent advances of electrochemical sensors for detecting and monitoring ROS/RNS. *Biosens. Bioelectron.* **2021**, *179*, 113052.

(18) Hasanzadeh, M.; Shadjou, N.; Guardia, M. D. L. Current advancement in electrochemical analysis of neurotransmitters in biological fluids. *TrAC Trends Anal. Chem.* **2017**, *86*, 107−121.

(19) Hosseini Sharifabad, A.; Safavi-Mirmahalleh, S.; Golshan, M.; Sienkiewicz, M.; Saeb, M. R.; Salami-Kalajahi, M. Metal-organic frameworks (MOFs)-based hybrid structures in developing glucose sensors. *Chem. Eng. J.* **2025**, *512*, 161513.

(20) Huang, X.; Liang, B.; Huang, S.; Liu, Z.; Yao, C.; Zheng, S.; Zhang, T.; Liu, Z.; Wang, Y.; Wu, Y.; Yang, J.; Liu, J.; Chen, H. J.; Xie, X. Vertical Graphene-Based Multiparametric Sensing Array for Integration of Smart Catheter to Electrochemically Monitor Peritoneal Dialysis. *Adv. Mater.* **2025**, *37* (3), 2412302.

(21) Qiao, Y.; Qiao, L.; Chen, Z.; Liu, B.; Gao, L.; Zhang, L. Wearable Sensor for Continuous Sweat Biomarker Monitoring. *Chemosensors.* **2022**, *10* (7), 273.

(22) Monteiro, T.; Almeida, M. G. Electrochemical Enzyme Biosensors Revisited: Old Solutions for New Problems. *Crit. Rev. Anal. Chem.* **2019**, *49* (1), 44−66.

(23) Tan, B.; Zhao, H.; Wu, W.; Liu, X.; Zhang, Y.; Quan, X. Fe_3O_4-AuNPs anchored 2D metal-organic framework nanosheets with DNA regulated switchable peroxidase-like activity. *Nanoscale.* **2017**, *9* (47), 18699−18710.

(24) Guliy, O. I.; Dykman, L. A. Prospects for the use of nanozyme-based electrochemical and colorimetric sensors for antibiotic detection. *Talanta.* **2025**, *286*, 127524.

(25) Wang, Z.; Hou, Y.; Tang, G.; Li, Y.; Zhao, Y.; Yu, Y.; Wang, G.; Yan, X.; Fan, K. Intelligent nanozymes: Biomimetic design, mechanisms and biomedical applications. *Fundamental Research.* **2025**, *5* (4), 1369−1383.

(26) Gong, C.; Wang, D.; Zhao, H. Biomimetic Metal-Pyrimidine Nanoflowers: Enzyme Immobilization Platforms with Boosted Activity. *Small.* **2023**, *19* (49), 2304077.

(27) Li, M.; Qiao, S.; Zheng, Y.; Andaloussi, Y. H.; Li, X.; Zhang, Z.; Li, A.; Cheng, P.; Ma, S.; Chen, Y. Fabricating Covalent Organic Framework Capsules with Commodious Microenvironment for Enzymes. *J. Am. Chem. Soc.* **2020**, *142* (14), 6675−6681.

(28) Cai, X.; Huang, Y.; Zhu, C. Immobilized Multi-Enzyme/Nanozyme Biomimetic Cascade Catalysis for Biosensing Applications. *Adv. Healthc. Mater.* **2025**, *14* (8), 2401834.

(29) Li, J.; Gao, M.; Xia, X.; Cen, Y.; Wei, F.; Yang, J.; Wang, L.; Hu, Q.; Xu, G. Spherical Hydrogel Sensor Based on PB@Fe-COF@Au Nanoparticles with Triplet Peroxidase-like Activity and Multiple Capture Sites for Effective Detection of Organophosphorus Pesticides. *ACS Appl. Mater. Interfaces.* **2023**, *15* (5), 6473−6485.

(30) Wu, B.; Zhang, G.; Ji, J.; Luo, R. H.; Chen, J.; Liu, F. L.; Coy, E.; Moya, S. E.; Li, Q.; Suo, X.; Chen, X.; Zheng, Y. T.; Li, Y.; Wang, G. ZIF-67-Derived Antivirus Cobalt Hydroxide LDH Nanosheets Produced through High-Concentration Cobalt Ion-Assisted Hydration. *Adv. Funct. Mater.* **2024**, *34* (14), 2312941.

(31) Zhu, Y.; Zhu, D.; Chen, Y.; Yan, Q.; Liu, C.; Ling, K.; Liu, Y.; Lee, D.; Wu, X.; Senftle, T.; Verduzco, R. Porphyrin-based donor-acceptor COFs as efficient and reusable photocatalysts for PET-RAFT polymerization under broad spectrum excitation. *Chem. Sci.* **2021**, *12*, 16092−16099.

(32) Wang, X.; Li, Y.; Chu, R.; Zhang, Z.; Hou, W.; Wang, L.; Li, L.; Zhang, P. Engineered an organic Z-scheme heterojunction of cu porphyrin-COF/g-C_3N_4 with planar covalent interaction for sustainable solar energy conversion. *Chem. Eng. J.* **2025**, *519*, 164922.

(33) Yang, Y.; Liu, J.; Gu, M.; Cheng, B.; Wang, L.; Yu, J. Bifunctional TiO_2/COF S-scheme photocatalyst with enhanced H_2O_2 production and furoic acid synthesis mechanism. *Appl. Catal. B Environ.* **2023**, *333*, 122780.
(34) Hayashi, K.; Mizuno, M.; Kandori, H.; Mizutani, Y. Cis-Trans Reisomerization Precedes Reprotonation of the Retinal Chromophore in the Photocycle of Schizorhodopsin 4. *Angew. Chem.-Int. Ed.* **2022**, *61* (33), No. e202203149.
(35) Sheng, H.; Wang, J.; Huang, J.; Li, Z.; Ren, G.; Zhang, L.; Yu, L.; Zhao, M.; Li, X.; Li, G.; Wang, N.; Shen, C.; Lu, G. Strong synergy between gold nanoparticles and cobalt porphyrin induces highly efficient photocatalytic hydrogen evolution. *Nat. Commun.* **2023**, *14* (1), 1528.
(36) Wu, S.; Deng, D.; Zhang, E.; Li, H.; Xu, L. CoN nanoparticles anchored on ultra-thin N-doped graphene as the oxygen reduction electrocatalyst for highly stable zinc-air batteries. *Carbon.* **2022**, *196*, 347−353.
(37) Zhang, C.; Cui, M.; Ren, J.; Xing, Y.; Li, N.; Zhao, H.; Liu, P.; Ji, X.; Li, M. Facile synthesis of novel spherical covalent organic frameworks integrated with Pt nanoparticles and multiwalled carbon nanotubes as electrochemical probe for tanshinol drug detection. *Chem. Eng. J.* **2020**, *401*, 126025.
(38) Chen, S.; Lo, W.; Huang, Y.; Si, X.; Liao, F.; Lin, S.; Williams, B. P.; Sun, T.; Lin, H.; An, Y.; Sun, T.; Ma, Y.; Yang, H.; Chou, L.; Shieh, F.; Tsung, C. Probing Interactions between Metal-Organic Frameworks and Freestanding Enzymes in a Hollow Structure. *Nano Lett.* **2020**, *20* (9), 6630−6635.
(39) Liang, W.; Xu, H.; Carraro, F.; Maddigan, N. K.; Li, Q.; Bell, S. G.; Huang, D. M.; Tarzia, A.; Solomon, M. B.; Amenitsch, H.; Vaccari, L.; Sumby, C. J.; Falcaro, P.; Doonan, C. J. Enhanced Activity of Enzymes Encapsulated in Hydrophilic Metal-Organic Frameworks. *J. Am. Chem. Soc.* **2019**, *141* (6), 2348−2355.
(40) van Soest, D. M. K.; Polderman, P. E.; den Toom, W. T. F.; Keijer, J. P.; van Roosmalen, M. J.; Leyten, T. M. F.; Lehmann, J.; Zwakenberg, S.; De Henau, S.; van Boxtel, R.; Burgering, B. M. T.; Dansen, T. B. Mitochondrial H_2O_2 release does not directly cause damage to chromosomal DNA. *Nat. Commun.* **2024**, *15* (1), 2725.
(41) Guo, J.; Wu, S.; Wang, Y.; Zhao, M. A label-free fluorescence biosensor based on a bifunctional MIL-101(Fe) nanozyme for sensitive detection of choline and acetylcholine at nanomolar level. *Sens. Actuators B: Chem.* **2020**, *312*, 128021.
(42) Loganathan, C.; Sakayanathan, P.; Thayumanavan, P. Astaxanthin-s-allyl cysteine diester against high glucose-induced neuronal toxicity *in vitro* and diabetes-associated cognitive decline *in vivo*: Effect on p53, oxidative stress and mitochondrial function. *Neurotoxicology.* **2021**, *86*, 114−124.
(43) Pena-Pereira, F.; Wojnowski, W.; Tobiszewski, M. AGREE-Analytical GREEnness Metric Approach and Software. *Anal. Chem.* **2020**, *92* (14), 10076−10082.
(44) Zhang, L.; Dang, X.; Li, T.; Zhao, H. Introducing oxygen vacancy in TiO/R-TiO_2 via non-stoichiometric engineering for chloride-resistant sensitive COD electrochemical detection. *Sens. Actuators B: Chem.* **2025**, *441*, 138044.
(45) Zhang, C.; Xia, Y.; Jiang, W.; Wang, C.; Han, B.; Hao, J. Determination of non-neuronal acetylcholine in human peripheral blood mononuclear cells by use of hydrophilic interaction ultra-performance liquid chromatography-tandem mass spectrometry. *J. Chromatogr. B* **2016**, *1022*, 265−273.
(46) Lamy, E.; Pilyser, L.; Paquet, C.; Bouaziz-Amar, E.; Grassin-Delyle, S. High-sensitivity quantification of acetylcholine and choline in human cerebrospinal fluid with a validated LC-MS/MS method. *Talanta.* **2021**, *224*, 121881.
(47) Beggel, S.; Kalis, E. J. J.; Geist, J. Towards harmonized ecotoxicological effect assessment of micro- and nanoplastics in aquatic systems. *Environ. Pollut.* **2025**, *366*, 125504.
(48) Jain, S. K.; Justin Margret, J.; Lally, M. Positive association of acetylcholinesterase (AChE) with the neutrophil-to-lymphocyte ratio and HbA1c, and a negative association with hydrogen sulfide (H_2S) levels among healthy African Americans, and H_2S-inhibition and high-glucose-upregulation of AChE in cultured THP-1 human monocytes. *Free. Radic. Biol. Med.* **2023**, *209*, 185−190.
(49) Duan, X.; Helal, M.; Wang, X.; Huang, Y.; Ebbesen, M. F.; Brewer, J.; Wang, S.; Wu, C.; Holbech, H.; Xu, E. G. Swim in Plastics: Clean Nanoplastics Cause Minimal Mortality but Alter Neuro-behavioral and Molecular Rhythms in Fish. *Environ. Sci. Technol.* **2025**, *59* (19), 9387−9398.
(50) Yan, L. Pathogenesis of Chronic Hyperglycemia: From Reductive Stress to Oxidative Stress. *J. Diabetes Res.* **2014**, *2014*, 137919.
(51) Manco, C.; Righi, D.; Locci, S.; Lucchese, G.; De Stefano, N.; Plantone, D. A Systematic Review Focusing on the Link between Engineered Nanoparticles and Neurodegeneration. *ACS Chem. Neurosci.* **2025**, *16* (8), 1420−1432.
(52) Sun, J.; Peng, S.; Yang, Q.; Yang, J.; Dai, Y.; Xing, L. Microplastics/nanoplastics and neurological health: An overview of neurological defects and mechanisms. *Toxicology.* **2025**, *511*, 154030.

https://doi.org/10.1021/envhealth.5c00556
Environ. Health 2026, 4, 1151−1161